The Planetary Science Journal, 6:13 (11pp), 2025 January https://doi.org/10.3847/PSJ/ad9606

Implications of Differentiated Late Accretion for the Volatile Inventory of the Bulk Silicate Earth

Damanveer S. Grewal[1,2] and Varun Manilal[2]
[1] School of Molecular Sciences, Arizona State University, Tempe, AZ 85281, USA; damanveer.grewal@asu.edu
[2] School of Earth and Space Exploration, Arizona State University, Tempe, AZ 85281, USA

Received 2024 August 17; revised 2024 October 30; accepted 2024 November 13; published 2025 January 16

Abstract

Earth is believed to have acquired its highly siderophile element (HSE) inventory through the late accretion of ∼0.3%–0.5% of its mass in chondrite-like materials, following the main stage of its growth. Late accretion, particularly if it originated from the outer solar system, could have significantly contributed to the bulk silicate Earth's (BSE = mantle + crust + hydrosphere + atmosphere) carbon–nitrogen–hydrogen (C–N–H) inventory. However, recent studies, noting differences between the HSE inventory of the Earth and Moon's mantle, suggest that relatively large lunar-sized differentiated impactors, rather than small chondritic projectiles, delivered HSEs to Earth's mantle during late accretion. The implications of a differentiated late accretion event for the BSE's C–N–H inventory remain unclear. In this study, we modeled the equilibrium partitioning of highly volatile C–N–H and moderately volatile sulfur–selenium–tellurium (S–Se–Te) between the atmosphere, magma ocean (MO), and core of lunar-sized or slightly larger impactors. The impactor's MO-degassed atmosphere contained most of its C–N–H inventory, whereas almost all of the S–Se–Te was present in its core or mantle. Given the low escape velocity of lunar-sized impactors, the MO-degassed atmosphere was likely dissipated quickly after core formation. As a result, in contrast to S–Se–Te, the contribution of differentiated late accretion to BSE's C–N–H inventory was limited, irrespective of its inner or outer solar system origin. The C–N–H-depleted nature of differentiated objects suggests that most of BSE's highly volatile inventory was delivered by primitive chondritic materials toward the final stages of Earth's accretion, before the Moon-forming event.

Unified Astronomy Thesaurus concepts: Earth (planet) (439); Solar system formation (1530); Planetary system formation (1257); Planetary science (1255)

1. Introduction

Earth experienced a protracted formation history, growing through the collisional accretion of planetesimals and planetary embryos over tens of millions of years (D. C. Rubie et al. 2011; N. Dauphas 2017). The main stage of its growth culminated in a giant impact that led to the formation of the Moon (R. M. Canup & E. Asphaug 2001; R. M. Canup 2004). Earth continued to accrete mass after the Moon-forming event. Evidence for this late accretion primarily comes from the "overabundance"—higher than expected based on metal/silicate partition coefficients during core formation—of highly siderophile elements (HSEs) in Earth's primitive mantle (K. Kimura et al. 1974; C.-L. Chou 1978; R. J. Walker 2009). The HSE excess, combined with the nearly chondritic relative abundances of HSEs, is explained by the addition of ∼0.3%–0.5% of Earth's mass (M_E) in chondritic material after core formation ceased, following the Moon-forming event (R. J. Walker 2009; J. M. D. Day et al. 2015; M. Fischer-Gödde et al. 2020). Considering the timing of the late accretion event, it is believed to have significantly contributed to the bulk silicate Earth's (BSE = mantle + crust + hydrosphere + atmosphere) inventory of moderately volatile elements like sulfur (S), selenium (Se), and tellurium (Te), as well as highly volatile elements such as carbon (C), nitrogen (N), and hydrogen (H) (F. Albarède 2009; Z. Wang & H. Becker 2013; N. Braukmüller et al. 2019; M. I. Varas-Reus et al. 2019). Therefore, late accretion not only provides fundamental insights into the dynamics of terrestrial planet growth but also could play a crucial role in constraining the origin of the life-essential volatiles in the BSE, and in turn, the Earth's habitability.

However, the provenance of late accretion materials (outer versus inner solar system) and, consequently, their contribution to the C–N–H budget of the BSE remains debated. For instance, Os and Ru isotope systematics of Earth's primitive mantle have been used to argue for a late accretion event composed of noncarbonaceous (NC) chondrites such as enstatite and ordinary chondrites, which have an inner solar system origin (T. Meisel et al. 1996; M. Fischer-Gödde & T. Kleine 2017), whereas positive ε^{100} Ru values in Eoarchean terrestrial rocks have been used to support the idea that late accretion was composed of carbonaceous (CC) chondrites, particularly CM chondrites, with an outer solar system origin (M. Fischer-Gödde et al. 2020). The relative abundances of S–Se–Te and mass-dependent Se isotopic variations in Earth's mantle also support the notion that late accretion materials had a CC reservoir origin (Z. Wang & H. Becker 2013; M. I. Varas-Reus et al. 2019). Since CC chondrites are generally enriched in highly volatile elements than their NC counterparts (M. M. Grady & I. P. Wright 2003; C. M. O. Alexander et al. 2012), the exact contribution of late accretion to the C–N–H budget of the BSE depends on whether its source material was NC or CC chondrites. For instance, late accretion involving 0.3%–0.5% M_E of CM chondrites could deliver ∼170%–280% of the N, ∼56%–94% of the H, and ∼20%–33% of the C inventory in the BSE. In contrast, a similar mass of EC

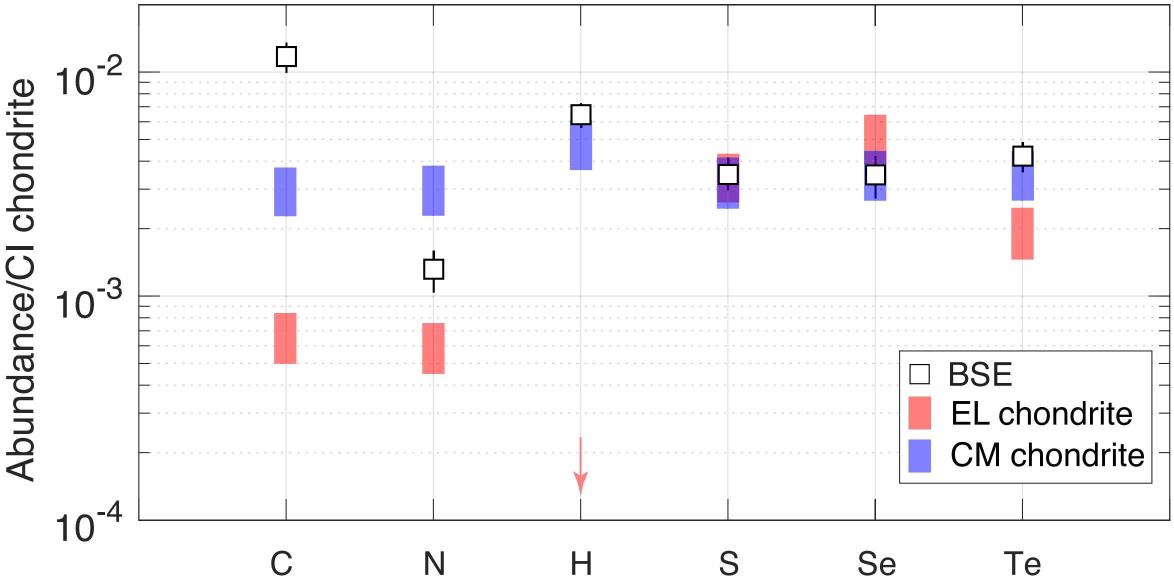

Figure 1. Comparison of C–N–H–S–Se–Te abundances in the BSE with the contribution of a chondritic late accretion event comprised of 0.3%–0.5% M_E of CM and EL chondrites. Data sources: (1) BSE: C (B. Marty et al. 2020); N and H (M. M. Hirschmann 2018); S, Se, and Te (Z. Wang & H. Becker 2013). (2) CM and EL chondrites: C, N, H, S, Se, and Te (C. M. O. Alexander 2022). Note that the H content of EL chondrites (represented by a downward-pointing arrow) is assumed to be near zero (C. M. O. Alexander 2022). The error bars for the BSE represent one standard deviation from the mean values. The shaded regions for CM and EL chondrites indicate the lower and upper bounds, based on contributions of 0.3% and 0.5% M_E, respectively, from chondritic materials.

chondrites would provide ∼34%–57% of the inventory of N and ∼4%–7% of the C in the BSE, but no H (Figure 1). Therefore, late accretion materials, especially if they were composed of volatile-rich CM and CI chondrites, could be an important source of life-essential volatiles, particularly N and H, in the BSE.

The idea that the late accretion originated from several chondritic projectiles has, however, been challenged (W. F. Bottke et al. 2010; R. Brasser et al. 2016; H. Genda et al. 2017; S. Marchi et al. 2018). The lunar mantle also has nearly chondritic relative abundances of HSEs, but its HSE inventory is lower by a factor of ∼35–40 compared to Earth's primitive mantle (J. M. D. Day et al. 2007). Based on this, Earth should have accreted ∼1900–2200 times the mass accreted by the Moon during late accretion. This number is ∼2 orders of magnitude higher than the Earth/Moon impact mass flux ratio of small objects, which directly reflects the ratios of their gravitational constants (W. F. Bottke et al. 2010). Therefore, late accretion via numerous small chondritic projectiles cannot explain the differences in HSE abundances between the Earth and Moon (W. F. Bottke et al. 2010). This discrepancy can be best explained if Earth accreted most of its late accretion mass via a few large impactors or, more statistically likely, from a large solitary lunar-sized or slightly larger impactor (W. F. Bottke et al. 2010; R. Brasser et al. 2016; H. Genda et al. 2017; S. Marchi et al. 2018).

Lunar-sized impactors, which are expected to accrete rapidly within the timescales of ^{26}Al decay, likely experienced large-scale melting followed by differentiation into a mantle and core (D. C. Rubie et al. 2011; H. Genda et al. 2017; S. Marchi et al. 2018). The HSE inventory of differentiated bodies is sequestered into their cores (R. J. Walker 2009). Impact simulations using the smooth particle hydrodynamics (SPH) method have shown that depending on the dynamics of the late accretion impact (e.g., impact angle and impact velocity), substantial portions of a differentiated impactor's core could either merge directly with Earth's core or be lost to space (H. Genda et al. 2017; S. Marchi et al. 2018). The portion of the impactor's core that got suspended in the Earth's mantle provided the required HSE inventory via rapid three-phase flow with solid silicate, molten silicate, and liquid metal followed by long-term mixing by mantle convection (J. Korenaga & S. Marchi 2023). Therefore, given the inefficient metal delivery, the HSE abundances in Earth's primitive mantle can be best explained if late accretion occurred through differentiated impactor(s) with a mass that was about 2–6 times higher (1%–3% M_E) than standard estimates (H. Genda et al. 2017; S. Marchi et al. 2018).

Late accretion via differentiated impactor(s) has important implications for its contribution to the C–N–H inventory in the BSE. In addition to being moderately siderophile, these elements are atmophile. Unlike refractory HSEs, the C–N–H content in a differentiated impactor's core and mantle is controlled by the equilibrium partitioning between the atmosphere, magma ocean (MO), and metallic melt (M. M. Hirschmann 2016; R. Dasgupta & D. S. Grewal 2019; D. S. Grewal et al. 2021b, 2022a, 2024a; M. M. Hirschmann et al. 2021; C. R. M. Jackson et al. 2021; Y. Li et al. 2023; K. Tsuno et al. 2024). The C–N–H content present in its mantle and core depends on the partial pressure of the respective species in its MO-degassed atmosphere, which is primarily influenced by its size. For a lunar-sized impactor, a substantial portion of the C–N–H inventory may reside in its MO-degassed atmosphere after differentiation (D. S. Grewal et al. 2021b, 2022a; Y. Li et al. 2023). Due to its low escape velocity and the strong extreme-ultraviolet (EUV) flux intensity of the young Sun (N. V. Erkaev et al. 2014; H. E. Schlichting et al. 2015; J. M. Y. Woo et al. 2019), a lunar-sized impactor would efficiently lose the volatiles present in its atmosphere during the MO stage (M. R. Benedikt et al. 2020). Consequently, if late accretion occurred through a differentiated body, its contribution to the volatile inventory of the BSE could be greatly suppressed, even if it originally accreted volatile-rich CC-chondrite-like materials. However, a quantitative approach to establish the consequences of a differentiated late accretion event on the BSE's volatile inventory is currently lacking.

In this study, we model the equilibrium partitioning of C–N–H between the atmosphere, MO, and core in differentiated impactors, using constraints from SPH simulations to determine the distribution of these elements among the constituent reservoirs. Additionally, we examine the partitioning of chalcophile elements S, Se, and Te, whose BSE inventory is also believed to be significantly influenced by the late accretion event (Z. Wang & H. Becker 2013; N. Braukmüller et al. 2019; M. I. Varas-Reus et al. 2019). The comparable yet distinct geochemical characteristics of these elements will help to develop a comprehensive understanding of the contribution of a differentiated late accretion event to the volatile inventory in the BSE.

2. Methods

2.1. Distribution of Volatiles between the Atmosphere, Mantle, and Core of the Impactor

We adopted the well-established framework of several previous studies to determine the equilibrium partitioning of volatiles between the atmosphere, MO, and core of the impactor (M. M. Hirschmann 2016; D. S. Grewal et al. 2021b, 2022a, 2024a; M. M. Hirschmann et al. 2021; C. R. M. Jackson et al. 2021; L. Shi et al. 2022; Y. Li et al. 2023; T.-A. Suer et al. 2023). The details are briefly summarized here. The total mass of a volatile element i participating in core, MO, and atmosphere equilibration in the impactor can be quantified using the following mass balance equation:

$$m_i^{\text{total}} = m_i^{\text{atm}} + m_i^{\text{MO}} + m_i^{\text{core}}. \tag{1}$$

The exchange of an element between the impactor's core and the postimpact MO is controlled by its equilibrium partition coefficient between metallic and silicate melt ($D_i^{\text{metal/silicate}}$; L. Rose-Weston et al. 2009; R. A. Fischer et al. 2020; D. S. Grewal et al. 2021b; S. Tagawa et al. 2021; see the Appendix for details). The exchange between the atmosphere and the underlying MO, provided it is well mixed, is quantified using a simplified solubility relationship in the form of Henry's law,

$$C_i^{\text{MO}} = S_i{\cdot}p_i, \tag{2}$$

where S_i is the Henrian constant for an element and p_i is the partial vapor pressure of the gaseous species of that element (M. M. Hirschmann 2016). The partial vapor pressure term is related to the mass of the vapor species in the atmosphere by

$$p_i = (m_{\text{i}}^{\text{atm}}.\, g.\, k_{\text{i}}.\, \mu/\mu_{\text{i}})/A. \tag{3}$$

Here, k_i is a mass factor that corrects for the difference between the mass of element i in the atmosphere and the mass of its gaseous species. g and A represent the impactor's gravitational constant and surface area, respectively. The factor μ/μ_i denotes the molar mass ratio of the average atmosphere and the gaseous species of element i. Combined, these equations yield the distribution of a volatile element between the atmosphere, MO, and core of the impactor. The relevant $D_i^{\text{metal/silicate}}$ and S_i values are determined using the parameterized equations from previous high pressure–temperature (P–T) experimental studies and are reported in the Appendix.

2.2. Choice of Parameters

2.2.1. Size of the Impactor

The mass of the impactor's core and mantle gravitationally bound to the postimpact Earth, primarily a function of the impact angle and velocity, has been estimated by two previous studies (H. Genda et al. 2017; S. Marchi et al. 2018). As the probability distribution of impact angles resembles a Gaussian curve, asteroids are most likely to strike a planetary surface at an angle close to 45°, making vertical and horizontal collisions highly improbable (D. L. Mathias et al. 2017). We used the results of the SPH simulations of H. Genda et al. (2017) and S. Marchi et al. (2018), where the fraction of the impactor's core retained in the Earth's mantle (f) was determined for the most probable impact angle of 45°. For instance, for an impactor with a metal/silicate ratio of 3:7 and impact velocity of $16\ \text{km s}^{-1}$, H. Genda et al. (2017) estimated an f value of ∼0.6, whereas S. Marchi et al. (2018) estimated an f value of ∼0.2 for an impactor with the same metal/silicate ratio but a higher impact velocity ($19\ \text{km s}^{-1}$). We directly utilize the estimates from both studies without taking a position on the reasons for their differences, which arise from variations in their SPH simulation setups.

The total mass of the impactor's core is calculated based on the portion of the impactor's core retained in Earth's mantle to account for the HSE inventory in the BSE. H. Genda et al. (2017) demonstrated that for an impact angle of 45°, a lunar-sized impactor could deliver the required abundances of HSEs to Earth's mantle. Since S. Marchi et al. (2018) estimated a lower fraction of the impactor's core to be retained in Earth's mantle, the total mass of the impactor(s) could be up to 3 times that of a lunar-sized impactor. This could mean either a single large impactor or multiple smaller ones (e.g., three lunar-sized impactors). In our calculations, we explore two end-member scenarios—a lunar-sized impactor (0.1% M_{E}) with an f value of 0.6 (H. Genda et al. 2017) and an impactor 3 times the mass of the lunar impactor (0.3% M_{E}) with an f value of 0.2 (S. Marchi et al. 2018). We will show that examining these end-member scenarios provides sufficient insight into the potential contribution of a differentiated late accretion event to the volatile inventory of the BSE.

2.2.2. Oxygen Fugacity

At the relatively low pressure of metal–silicate equilibration in lunar-sized or slightly larger impactors, the partition coefficient of the volatile elements between metallic and silicate melts ($D_i^{\text{metal/silicate}}$) is primarily controlled by the oxygen fugacity ($f\text{O}_2$) of metal–silicate melt equilibration at the base of the MO (H. Chi et al. 2014; C. Dalou et al. 2017; K. Tsuno et al. 2018; D. S. Grewal et al. 2019a, 2021a, 2022b; I. M. Speelmanns et al. 2019; Y. Li et al. 2023, 2016, 2015). Similarly, the Henrian solubility coefficient (S_{i}) for C–N–H is controlled by the $f\text{O}_2$ of vapor–silicate melt exchange at the surface of the MO (M. M. Hirschmann 2016; T.-A. Suer et al. 2023). Since there are no vertical $f\text{O}_2$ gradients in the relatively shallow MOs of lunar-sized rocky bodies (J. Deng et al. 2020), the $f\text{O}_2$ of vapor–silicate melt exchange is roughly similar to the $f\text{O}_2$ of metal–silicate equilibration. Given the debate over the provenance of late accretion (NC versus CC reservoir), the exact $f\text{O}_2$ of metal–silicate melt equilibration in the impactor remains uncertain. For instance, the $f\text{O}_2$ of metal–silicate melt equilibration in reduced bodies emanating from the inner solar system could be as reduced as IW–4, whereas that of oxidized bodies emanating from the outer solar system could be up to

IW–1 (D. C. Rubie et al. 2011). Due to the uncertainty in this parameter and its influence on $D_i^{\mathrm{metal/silicate}}$ and S_i values, we explore three $f\mathrm{O}_2$ values of metal–silicate melt equilibration: IW–4, IW–2, and IW–1. The range of $f\mathrm{O}_2$ values considered is based on previously reported values for Earth's core–mantle differentiation (IW−2) and those of reduced (IW−4) and oxidized (IW−1) planetary embryos that accreted to form Earth (D. C. Rubie et al. 2011, 2015).

2.2.3. Abundances of Volatiles in the Bulk Impactor

Planetesimals and small planetary embryos are prone to open system loss of C–N–H during thermal evolution, driven by the heat released from the decay of ^{26}Al (N. Sugiura et al. 1986; K. Hashizume & N. Sugiura 1998; R. R. Fu et al. 2017; D. S. Grewal 2022; D. S. Grewal et al. 2022a). Evidence from chondrites indicates that most of the primordial C–N–H inventory is lost before the onset of metal and silicate melting (D. S. Grewal 2022; D. S. Grewal & P. D. Asimow 2023; M. E. Newcombe et al. 2023; L. D. Peterson et al. 2023a, 2024; D. S. Grewal et al. 2024b). For instance, the C and N inventory of chondrites decreases sharply with increasing peak metamorphic temperature (C. M. O. Alexander et al. 1998; V. K. Pearson et al. 2006; D. S. Grewal 2022; D. S. Grewal et al. 2022a, 2025). The steepest decline occurs at temperatures below 300°C, where 90%–99% of the primordial C and N inventory is lost due to the disintegration of the soluble organic matter, composed of amino acids, sugar derivatives, nucleobases, and various polyaromatic hydrocarbon compounds (C. M. O. Alexander et al. 1998; M. A. Sephton et al. 2003; C. Le Guillou et al. 2014; D. I. Foustoukos et al. 2021; D. S. Grewal et al. 2022a). Similarly, almost all primordial H_2O is lost due to the efficient ascent of free volatiles in the gas and supercritical fluid phases, first by the melting of ice into water and then by the progressive destruction of hydrated minerals at higher temperatures (R. R. Fu & L. T. Elkins-Tanton 2014; T. Lichtenberg et al. 2019; M. E. Newcombe et al. 2023). Positively buoyant C–N–H-bearing fluids can migrate toward the surface of protoplanets within tens to hundreds of years (N. Sugiura et al. 1986; K. Hashizume & N. Sugiura 1998). This period, much shorter than the time required for the formation of alloy and silicate melts, can result in the efficient removal of C–N–H-bearing fluids from protoplanetary interiors before core formation begins. Magmatic iron meteorites, remnants of the metallic cores of the earliest solar system protoplanets, also record C- and N-poor conditions within protoplanetary interiors during core formation (D. S. Grewal et al. 2021c, 2022a, 2022b, 2025; D. S. Grewal & P. D. Asimow 2023). Therefore, regardless of whether these percolated volatiles are lost to space or trapped in near-surface layers, protoplanetary interiors were volatile-depleted before atmosphere, MO, and core equilibration.

Relatively large protoplanetary bodies, such as lunar-sized planetary embryos, formed within ∼1–2 Myr of solar system formation, i.e., during the period when ^{26}Al was extant (S. J. Weidenschilling 2011, 2019). It is therefore highly likely that the late accretion impactor also experienced similar heating processes experienced by early protoplanetary bodies. To account for open system C–N–H loss prior to the onset of large-scale melting, we assume the bulk C–N–H inventory during atmosphere–MO–core equilibration to be 10% of CM chondrites. This relatively optimistic estimate is based on the correlation between the C and N content of thermally metamorphosed chondrites (M. M. Grady & I. P. Wright 2003; V. K. Pearson et al. 2006; D. S. Grewal et al. 2022a) and is at least an order of magnitude higher than the bulk N and C inventory of protoplanetary interiors during core–mantle differentiation, as inferred from magmatic iron meteorites (D. S. Grewal et al. 2022a, 2025; D. S. Grewal & P. D. Asimow 2023). To assess the sensitivity of our calculations to this parameter, we conducted additional sets of calculations using an unrealistically high bulk C–N–H inventory in the impactor (50% of CM chondrites). In contrast, since troilite—the main carrier of S, Se, and Te in chondrites—is refractory, these moderately volatile elements are resistant to loss during thermal metamorphism. As a result, their bulk inventory is assumed to be chondritic.

3. Results

In a lunar-sized impactor, most of the C–N–H inventory in the impactor was present in its MO-degassed atmosphere, regardless of the $f\mathrm{O}_2$ of metal–silicate equilibration (Figure 2(A)). For instance, ∼92%–99% of the C, ∼97%–98% of the N, and ∼98%–99% of the H in the impactor resided in its MO-degassed atmosphere, with the remainder in the core, except at IW–4, where the impactor's MO contained ∼2% of the bulk N inventory. The latter is due to the decrease in $D_{\mathrm{N}}^{\mathrm{metal/silicate}}$ and increase in N solubility in the silicate melt with decreasing $f\mathrm{O}_2$ (G. Libourel et al. 2003; C. Dalou et al. 2017; D. S. Grewal et al. 2019a, 2020, 2021b; I. M. Speelmanns et al. 2019; F. Bernadou et al. 2021; R. Dasgupta et al. 2022). The C and H inventory in the core increases as $f\mathrm{O}_2$ decreases due to a rise in their respective metal–silicate partition coefficients (Figure 3). In contrast, the N inventory in the core remains unchanged because the opposite effects of $D_{\mathrm{N}}^{\mathrm{metal/silicate}}$ and N solubility in the silicate melt offset each other as $f\mathrm{O}_2$ decreases. The C–N–H inventory in the impactor's MO was $\ll$1%, except for N at IW–4. In contrast, the high solubility of S–Se–Te in silicate melts combined with their moderately siderophile character results in most of their inventory residing in their core and MO. For instance, at IW–2 and IW–1, ∼97%–99% and ∼1%–2% of the S–Se–Te in the impactor resided in its core and MO, respectively, while <1% was present in its MO-degassed atmosphere, whereas at IW–4, the S–Se–Te inventory in the impactor's core is significantly lower. For instance, ∼74%–87% of the S–Se–Te in the impactor resided in its core, while ∼8%–17% and ∼4%–8% resided in its MO and MO-degassed atmosphere, respectively. This is because of the lower metal–silicate partition coefficients of S–Se–Te at IW–4 (Figure 3). Although our calculations were conducted at a fixed metal–silicate equilibration temperature of 2200 K (N. Rai & W. Van Westrenen 2014), our predictions remain robust due to the siderophile character of C–N–H and S–Se–Te across a reasonable range of temperatures relevant for metal–silicate equilibration in a lunar-sized impactor (Figure A1).

Comparable conclusions can be drawn for an impactor 3 times the mass of a lunar-sized impactor (Figure 2(B)). The larger size leads to increased solubility of volatile species in the silicate melt because their partial pressure scales with the impactor's radius and gravitational constant (M. M. Hirschmann 2016, D. S. Grewal et al. 2024a). Consequently, more C–N–H dissolve into the MO of the larger impactor (0.3% M_{E}) at a fixed $f\mathrm{O}_2$, making more available for fractionation between MO and alloy melts, allowing a higher proportion to segregate into the core. For instance, C–N–H inventory in the core approximately doubles compared to the lunar-sized impactor. It should be noted that the MO-degassed atmosphere, containing

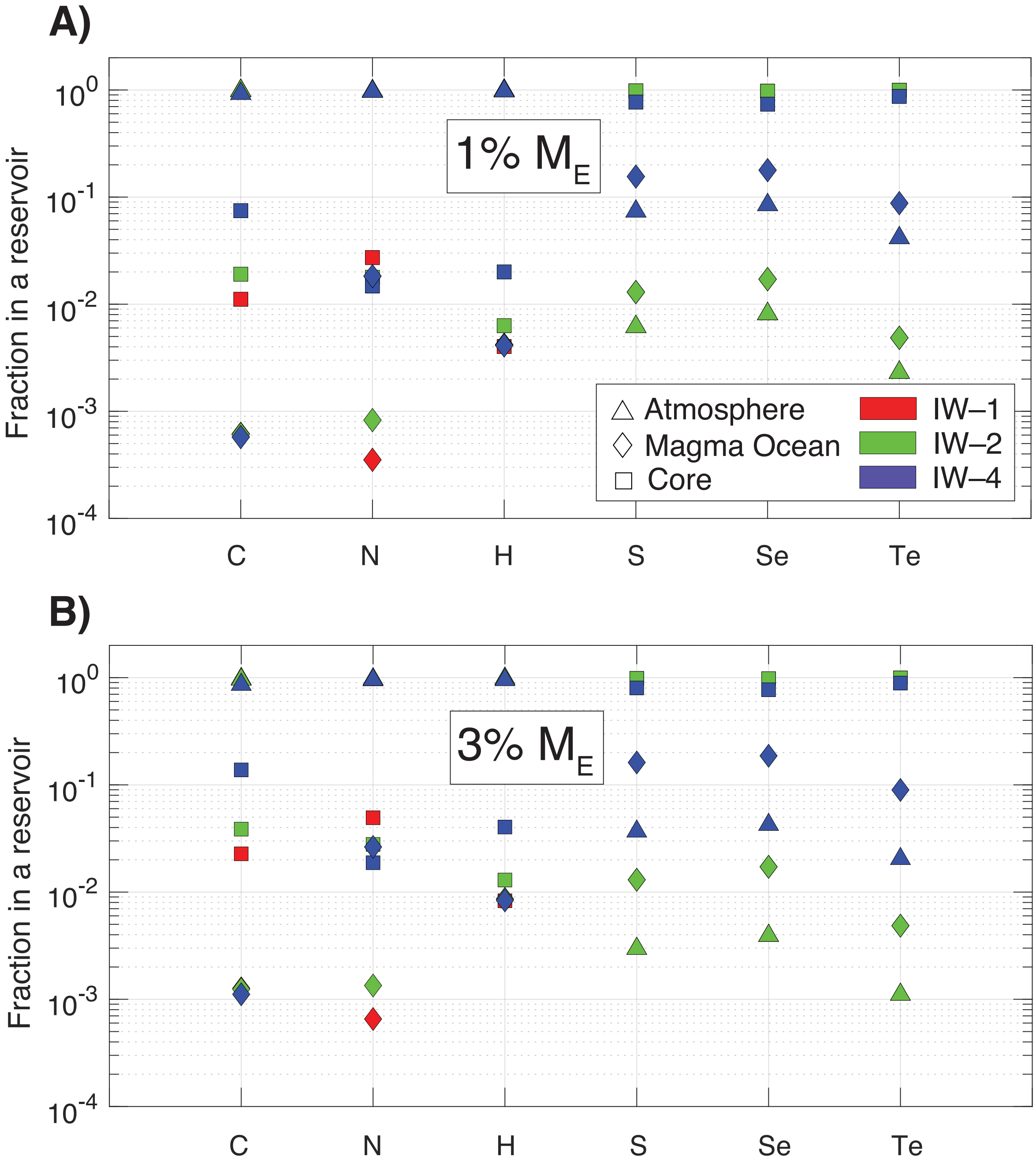

Figure 2. Fractional distribution of C–N–H–S–Se–Te between the atmosphere, MO, and core of a (A) 1% M_E and (B) 3% M_E impactor at IW–4, IW–2, and IW–1. The impactor's MO-degassed atmosphere contains the majority of the C–N–H inventory, whereas most of the S–Se–Te resides in its core. Note that the symbols for C–N–H and S–Se–Te overlap at IW–2 and IW–1.

~86%–98% of the C, ~95%–97% of the N, and ~95%–98% of the H, still remains the primary C–N–H reservoir. The distribution of S–Se–Te inventory in the impactor at IW–2 and IW–1, where <1% of these elements were present in the MO-degassed atmosphere, remains practically unchanged, whereas at IW–4, the S–Se–Te inventory in the MO-degassed atmosphere was lowered to ~2%–4%.

4. Discussion

4.1. Contribution of the Late Accretion Impactor to the C–N–H Inventory of the BSE

The distribution of volatiles between the atmosphere, MO, and core of the impactor can help determine its contribution to the C–N–H inventory of the BSE. Most of the impactor's C–N–H inventory was in its MO-degassed atmosphere (Figure 2). As a result, the amount of C–N–H a differentiated impactor could deliver to the BSE during late accretion was largely determined by the fate of the MO-degassed atmosphere prior to the late accretion event. Numerical models predict that a lunar-sized planetary embryo would rapidly lose its atmosphere when subjected to a hot MO (M. R. Benedikt et al. 2020; E. D. Young et al. 2023). With the outgassing flux nearly matching the escape rate, maintaining a stable hydrostatic equilibrium of the atmosphere becomes unlikely (M. R. Benedikt et al. 2020; H. Lammer et al. 2020). In such conditions, the limited gravity of a lunar-sized impactor is insufficient to prevent the MO-degassed atmosphere from dissipating into

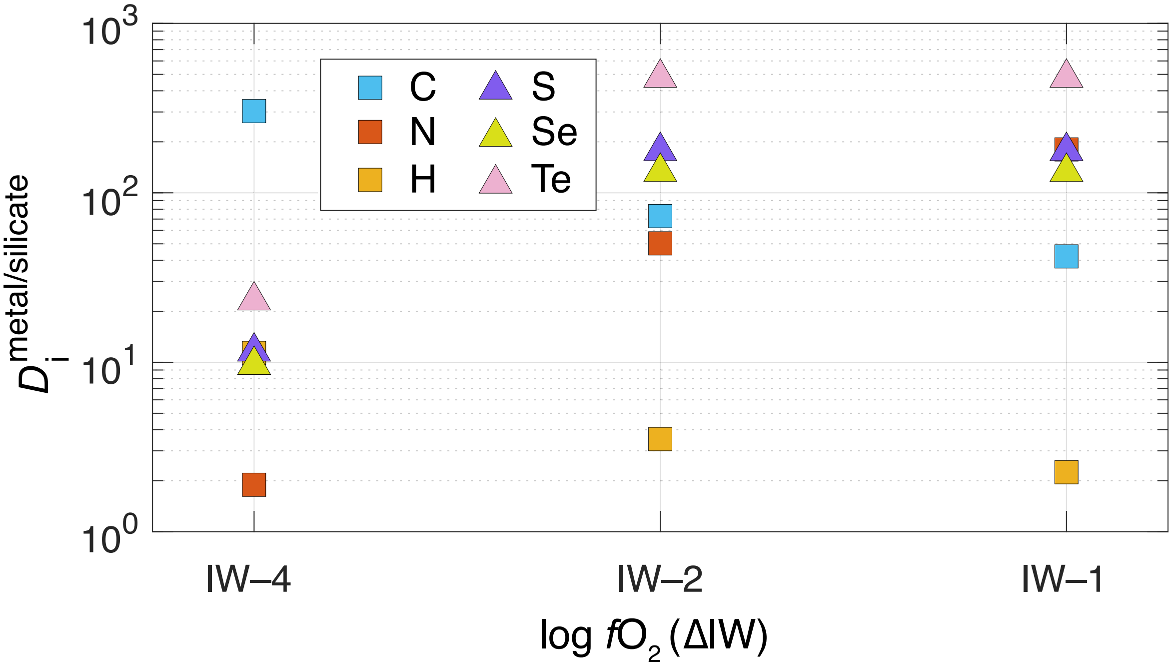

Figure 3. $D_i^{\mathrm{metal/silicate}}$ values of C–N–H and S–Se–Te at IW−4, IW−2, and IW−1. The $D_i^{\mathrm{metal/silicate}}$ of C and H increase with decreasing $f\mathrm{O}_2$, whereas those of N decrease. The $D_i^{\mathrm{metal/silicate}}$ values of S–Se–Te are broadly similar at IW−2 and IW−1, whereas those at IW−4 are an order of magnitude lower.

space. Additionally, the strong EUV flux from the young Sun would accelerate atmospheric loss, resulting in the rapid loss of the MO-degassed atmosphere (N. V. Erkaev et al. 2014; H. E. Schlichting et al. 2015; J. M. Y. Woo et al. 2019). Therefore, it can be safely assumed that the MO-degassed atmosphere component from the late accretion impactor did not contribute to the C–N–H inventory of the BSE. This assumption aligns with several previous studies on the Earth's main accretion phase, where the MO-degassed component in lunar- to Mars-sized seed planetary embryos is considered lost before they accreted to Earth (I. M. Speelmanns et al. 2019; D. S. Grewal et al. 2021b, 2024a; C. R. M. Jackson et al. 2021; Y. Li et al. 2023).

The contribution of the impactor's core and mantle to the C–N–H inventory of the BSE can be traced using the results of the SPH simulations by H. Genda et al. (2017) and S. Marchi et al. (2018). The former suggested that ∼60% and ∼64% of a lunar-sized impactor's core and mantle, respectively, was incorporated into the Earth's mantle. For an impactor 3 times the mass of the lunar-sized one, the latter study indicates that only ∼20% and ∼40% of its core and mantle, respectively, was retained in Earth's mantle. Since nearly all of the impactor's C–N–H inventory, excluding its MO-degassed atmosphere, was concentrated in its core, tracking the core component alone is enough to constrain its contribution to the C–N–H inventory of the BSE. The contribution from the MO component for N was also considered when the impactor underwent metal–silicate equilibration at IW−4. Across all considered $f\mathrm{O}_2$ scenarios, a lunar-sized impactor containing 10% of CM chondrite bulk C–N–H could deliver ∼0.04%–0.3% of the C, ∼1%–3% of the N, and ∼0.1%–0.3% of the H inventory of the BSE (Figure 4(A)). In comparison, the larger impactor could deliver slightly higher amounts—∼0.1%–0.5% of the C, ∼2%–6% of the N, and ∼0.3%–0.7% of the H in the BSE (Figure 4(B)). Even after considering an unrealistically high bulk C–N–H inventory in the impactor—50% of CM chondrites—in our models, the impactor's contribution during late accretion to the C–N–H inventory remained limited. For instance, a lunar-sized impactor would deliver ∼0.2%–2% of the C, ∼3%–6% of the N, and 0.5%–1% of the H in the BSE (Figure 4(A)), whereas the larger impactor delivered ∼0.5%–3% of the C, ∼5%–14% of the N, and ∼2%–3% of the H in the BSE (Figure 4(B)). Due to the chondritic abundances of the moderately volatile elements S, Se, and Te in the bulk impactor and with most of these elements concentrated in its core, the late accretion impactor could account for the entire S–Se–Te inventory of the BSE. For example, a lunar-sized impactor could contribute ∼120%–150% of the S–Se–Te inventory of the BSE, while a larger impactor could contribute around ∼130%–180%. The excess delivery of S–Se–Te by the late accretion impactor is tied to the CM-chondrite-like abundances of these elements used in our calculations. This discrepancy could be resolved if the bulk S–Se–Te levels in the impactor were more in line with the relatively volatile-depleted CO and CV chondrites.

Our results demonstrate that a differentiated late accretion event contributed little to the C–N–H inventory of the BSE (Figure 4). Even though we presented results for only two end-member impactors (0.1% and 0.3% M_{E}), our conclusions remain applicable for other intermediate scenarios. For instance, based on the results of S. Marchi et al. (2018), if instead of a single large impactor (0.3% M_{E}), multiple smaller impactors (such as three lunar-sized impactors) were responsible for providing the HSE inventory of the BSE, the contribution to the C–N–H inventory would still be limited. Variations in the impactor's bulk C–N–H inventory and its $f\mathrm{O}_2$ during metal–silicate equilibration also do not significantly affect our conclusions (Figure 4). Therefore, regardless of whether the differentiated impactor originated from the inner or outer solar system, it could not significantly contribute to the C–N–H inventory of the BSE, provided that its MO-degassed atmosphere was lost before the late accretion event. As previously discussed, this is a fairly robust assumption supported by several geophysical and

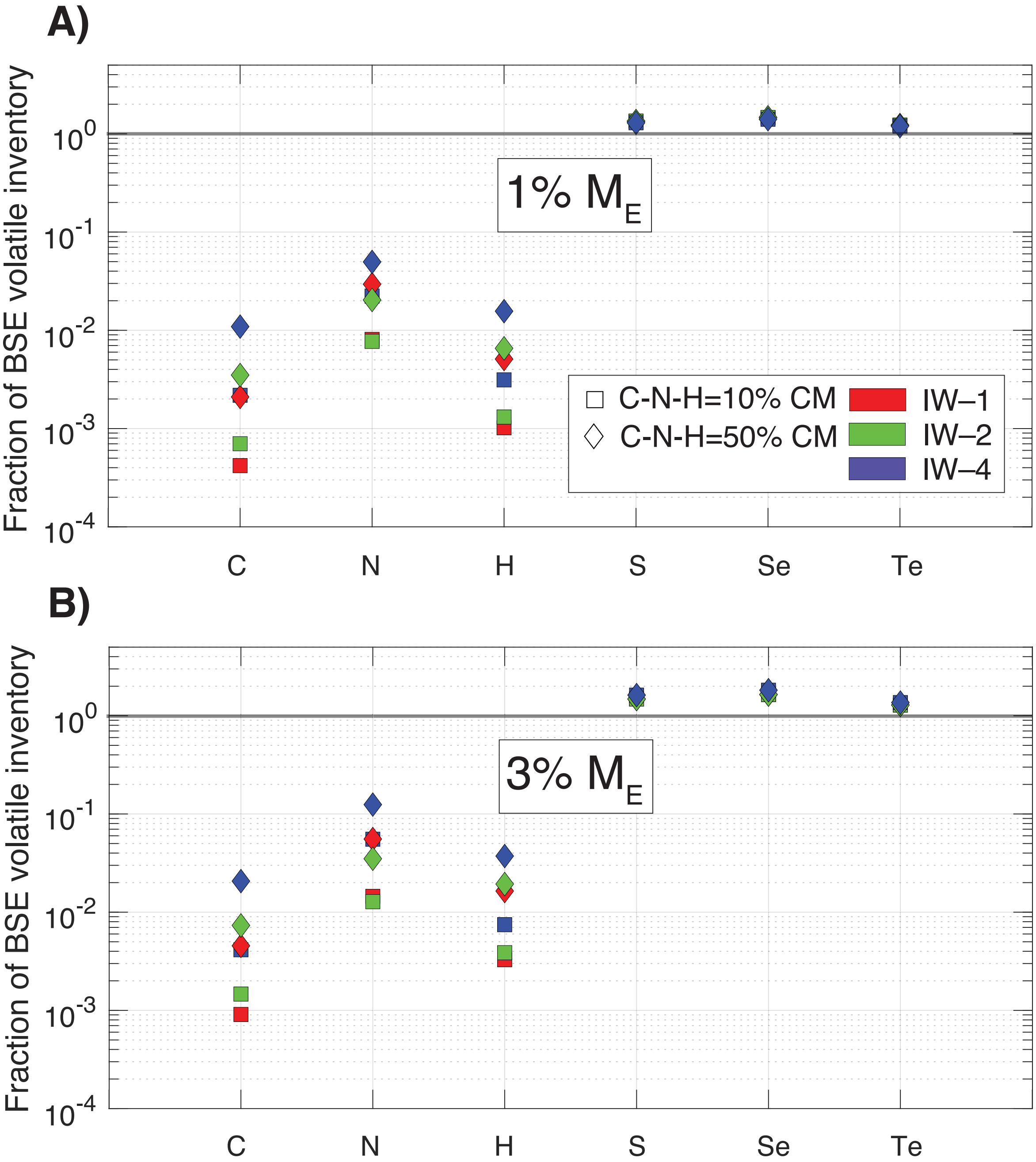

Figure 4. Contribution of differentiated late accretion via a (A) 1% M_E and (B) 3% M_E impactor to the C–N–H–S–Se–Te of the BSE at IW–4, IW–2, and IW–1. The contribution to the C–N–H inventory of the BSE was limited, whereas the entire S–Se–Te inventory could be established. Note that the symbols for S–Se–Te overlap.

geochemical arguments. Evidence for the C–N–H-depleted nature of the cores and mantles of differentiated protoplanetary bodies is evident in the meteorite record. For instance, the cores of magmatic iron meteorite parent bodies (up to 1000 km in diameter) are extremely C- and N-poor (D. S. Grewal et al. 2022a, 2025; D. S. Grewal & P. D. Asimow 2023). Angrites, aubrites, howardite–eucrite–diogenite, and other primitive and differentiated achondrites also indicate C–N–H-depleted mantles in early differentiated bodies (A. R. Sarafian et al. 2017; F. A. J. Abernethy et al. 2018; M. E. Newcombe et al. 2023; L. D. Peterson et al. 2023b, 2024). If a lunar-sized impactor formed from the collisional accretion of such smaller bodies, its core and mantle would likely have even less C–N–H inventory than the optimistic scenarios considered in this study.

4.2. When Was the C–N–H Inventory of the BSE Delivered?

The findings of this study suggest that in the scenario of late accretion via differentiated impactor(s), the majority of the C–N–H inventory in the BSE must have been delivered before the late accretion event. Previous studies proposed that the Moon-forming impactor could have been the primary source of the BSE's C–N–H inventory (G. Budde et al. 2019; D. S. Grewal et al. 2019b). However, the growth of a Mars-sized Moon-forming impactor through collisions of differentiated planetesimals and Moon-sized planetary embryos, which are prone to significant volatile loss during thermal metamorphism and melting (D. S. Grewal 2022; D. S. Grewal et al. 2022a, 2025; D. S. Grewal & P. D. Asimow 2023; M. E. Newcombe et al. 2023; L. D. Peterson et al. 2023b, 2024), raises doubts about its role as the primary source of volatiles in the BSE. A recent study (D. S. Grewal et al. 2024a) accounting for the updated C inventory in the BSE (B. Marty et al. 2020), substantial differences in the fO_2 between atmosphere–MO interactions and metal–silicate equilibration within deep MOs (K. Armstrong et al. 2019; M. M. Hirschmann 2022; H. Kuwahara et al. 2023), and advancements in the understanding of C–N–H partitioning behavior under extreme pressures and temperatures (T. A. Suer et al. 2017; S. Tagawa et al. 2021; I. Blanchard et al. 2022; D. Huang et al. 2024) has shown that the Moon-forming impactor was unlikely to be the primary source of volatiles in the BSE. Since Earth primarily formed from differentiated planetary embryos, and if these embryos were similarly depleted in volatiles, most of the C–N–H inventory in the BSE—especially the relatively abundant C and H—must be attributed to the accretion of volatile-rich, chondrite-like primitive materials (D. S. Grewal et al. 2024a). These materials were likely accreted during the later stages of Earth's accretion, likely before the Moon-forming event, when the proto had grown large enough (~90% M_E) to gravitationally retain its atmospheric C–N–H inventory (D. S. Grewal et al. 2024a). Some degree of processing of these materials would be required to account for the nonchondritic C/N and C/H ratios observed in the BSE. Crucially, any C–N–H delivered via undifferentiated materials would need to survive segregation into Earth's core during metal–silicate equilibration in the Moon-forming event. Recent studies predict that the majority of the impactor's core directly merges with Earth's core during the Moon-forming giant impact, resulting in limited metal–silicate equilibration (M. Landeau et al. 2021; M. Nakajima et al. 2021). Thus, C–N–H delivered before the Moon-forming event may largely avoid segregation into Earth's core during the giant impact and remain in the BSE.

Since undifferentiated materials would have contributed significant amounts of S–Se–Te, along with C–N–H, to the BSE before the Moon-forming event, a lack of metal–silicate equilibration during the Moon-forming event would have led to an excess of S–Se–Te in the BSE. This is because lunar-sized differentiated impactor(s) have the potential to deliver the entire S–Se–Te inventory of the BSE during the late accretion event (Figure 4). The S–Se–Te excess in the BSE could be avoided if these elements were efficiently segregated into the Earth's core through the widespread exsolution and segregation of iron sulfide liquid from the silicate melt (the Hadean matte) during the cooling and crystallizing of the MO after the Moon-forming event (H. St C. O'Neill 1991; V. Laurenz et al. 2016). Alternatively, the mass of materials added during the late accretion event may have been lower than current estimates suggest. Recent studies considering the pre-late-accretion component of HSEs in Earth's mantle suggest that the mass added during the late accretion event could be ~0.3% M_E (M. Fischer-Gödde et al. 2020). Based on constraints from noble gases, C. M. O. Alexander (2022) predicted a late accretion mass of ~0.2% M_E. This reduction in the estimated late accretion mass is supported by the decrease in metal–silicate partition coefficients of HSEs at high pressures during the final stages of Earth's core formation (U. Mann et al. 2012), which would help in the retention of HSEs in Earth's mantle after core formation ceased following the Moon-forming event. The relative fractionation of HSEs further supports this evidence (V. Laurenz et al. 2016; D. C. Rubie et al. 2016). The nonchondritic sulfur isotope signature of Earth's primitive mantle also suggests that late accretion was not the sole source of S–Se–Te in the BSE (J. Labidi et al. 2013). A diminished role for the late accretion event in shaping the HSE inventory of the BSE could help resolve several inconsistencies related to the establishment of the S–Se–Te inventory in the BSE.

5. Conclusions

In this study, we explored the contribution of a differentiated late accretion event to the C–N–H and S–Se–Te inventories of the BSE. Our calculations indicate that during atmosphere, MO, and core equilibration, the majority of the C–N–H inventory in differentiated late impactors relevant to the late accretion event is concentrated in their atmosphere. For example, the MO-degassed atmosphere of a lunar-sized impactor contains ~92%–99% of its C, N, and H inventory, with the remainder primarily residing in the core, except for N during metal–silicate equilibration at IW–4, where the nonatmosphere N inventory is almost equally distributed between the core and MO. For an impactor 3 times the mass of a lunar-sized one, although the C–N–H inventory in nonatmosphere reservoirs nearly doubles, the MO-degassed atmosphere remains the dominant C–N–H reservoir, containing ~86%–98% of the bulk C–N–H inventory.

Given the relatively low escape velocity of lunar-sized or slightly larger impactors, the MO-degassed atmosphere was likely lost long before the late accretion event, which could have occurred up to ~100 million yr after the formation of the solar system. Due to the C–N–H-poor nature of their cores and mantles, the contribution of a differentiated late accretion event to the BSE's C–N–H inventory was limited. In contrast, because the majority of S–Se–Te was present in the impactor's core, late accretion could potentially deliver the entire inventory of these elements to the BSE. Therefore, if late accretion occurred through differentiated impactors, it was not a significant source of the C–N–H inventory in the BSE, regardless of whether the impactors originated from the inner or outer solar system. The C–N–H-depleted nature of differentiated objects suggests that most of Earth's C–N–H inventory was delivered by a small amount of primitive chondritic material during the final stages of Earth's accretion, prior to the Moon-forming event. Meanwhile, the S–Se–Te inventory of the BSE was influenced by both pre-late accretion and late accretion events.

Acknowledgments

Amrita P. Vyas is thanked for improving the clarity of our communication. We thank two anonymous reviewers for the critical comments, which helped us improve several aspects of our communication. This research was supported by startup funds from ASU to DSG.

Appendix

A1. Metal/Silicate Partition Coefficients

1. C: $\log D_C^{\text{alloy/silicate}} = 1.49 + \frac{3000}{T} - 235\,\frac{P}{T} + 9.6\log_{10}(1 - X_S^{\text{alloy}}) - 19.5\ \log_{10}(1 - X_O^{\text{alloy}}) - 0.118\ \text{NBO}/T - 0.238\ \log fO_2$ (IW) (R. A. Fischer et al. 2020).
2. N: $\ln\ D_N^{\text{alloy/silicate}} = 7513.54 + \frac{9813.37}{T} - 68.24\ \frac{P}{T} + 362.16\ \ln\ (100 - X_S^{\text{alloy}}) - 39.87\ \ln\ (100 - X_S^{\text{alloy}})^2 - 0.25\ \ln\ (100 - \mathrm{X}_{Si}^{\text{alloy}})^2 - 3596.39\ \ln\ (100 - X_C^{\text{alloy}}) +$

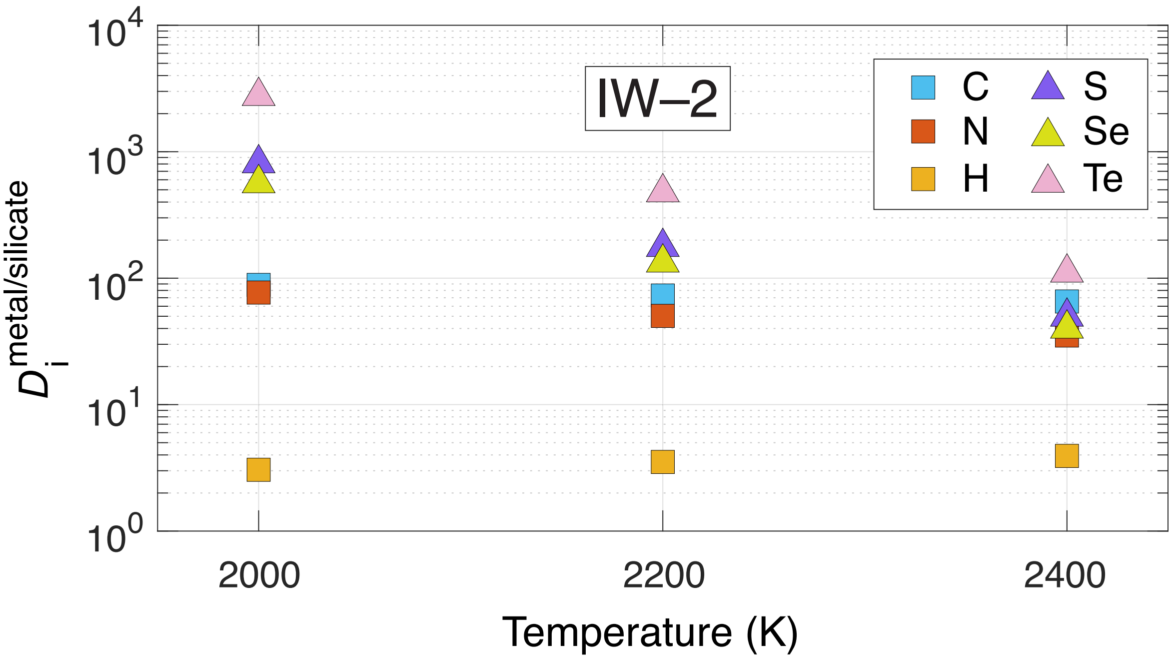

Figure A1. C–N–H and S–Se–Te show siderophile character across a reasonable range of temperatures relevant for metal–silicate equilibration in a lunar-sized impactor.

397.32 ln $(100 - X_C^{\mathrm{alloy}})^2$ + 0.84 NBO/T + 1.40 ln $X_{\mathrm{FeO}}^{\mathrm{silicate}}$ (D. S. Grewal et al. 2021b).

3. H: $\log K_D^H = 2.42 - \frac{2892}{T} - 32\,\frac{P}{T}$ (S. Tagawa et al. 2021).
4. S: $\log D_S^{\mathrm{metal/silicate}} = -4.37 + \frac{13,686}{T} + 217.49\frac{P}{T}$ (L. Rose-Weston et al. 2009).
5. Se: $\log D_{\mathrm{Se}}^{\mathrm{metal/silicate}} = -4.15 + \frac{12,545}{T} + 313.9\,\frac{P}{T}$ (L. Rose-Weston et al. 2009).
6. Te: $\log D_{\mathrm{Te}}^{\mathrm{metal/silicate}} = -4.94 + \frac{15,069}{T} + 422.98\,\frac{P}{T}$ (L. Rose-Weston et al. 2009).

We opted to use the parameterized equation for S from L. Rose-Weston et al. (2009) instead of the more recent equations by A. Boujibar et al. (2014) and T. A. Suer et al. (2017) for two main reasons: (1) the parameterized equations for Se and Te provided by L. Rose-Weston et al. (2009) are similar to that of S, helping to prevent any numerical artifacts in our calculations, and (2) these equations were based on experimental data collected at P–T conditions that are directly relevant to the lunar-sized impactors studied here. It is important to note that the parameterized equations for S, Se, and Te can only be applied at $\log f\mathrm{O}_2 >$ IW–2. Since there are no parameterized equations for Se and Te at IW–4, the $D_i^{\mathrm{metal/silicate}}$ values for all three elements, based on the experimental data of L. Rose-Weston et al. (2009), are assumed to be an order of magnitude lower than those at IW–2 and IW–1.

Here are the values of the parameters used in the $D_i^{\mathrm{metal/silicate}}$ equations: $P = 4$ GPa and $T = 2200$ K (based on metal–silicate equilibration in the Moon; N. Rai & W. Van Westrenen 2014); $X_O^{\mathrm{alloy}} = 0$; X_S^{alloy} was calculated using $D_S^{\mathrm{metal/silicate}}$; X_C^{alloy} was calculated using $D_C^{\mathrm{alloy/silicate}}$; $\log f\mathrm{O}_2$ = IW–4, IW–2, and IW–1; $X_{\mathrm{FeO}}^{\mathrm{silicate}} = 0.65$, 6.33, and 15.57; $X_{\mathrm{Si}}^{\mathrm{alloy}} = 1.2$, 0, and 0. The range of $f\mathrm{O}_2$ values considered is based on previously reported values for Earth's core–mantle differentiation (IW−2) and those of reduced (IW−4) and oxidized (IW−1) planetary embryos that accreted to form Earth (D. C. Rubie et al. 2011, 2015). In Figure 3 and A1, we have shown the variation of $D_i^{\mathrm{metal/silicate}}$ as a function of $f\mathrm{O}_2$ and temperature of metal–silicate equilibration, respectively.

A2. Solubilities in Silicate Melts

Using the method outlined by D. S. Grewal et al. (2022a), the exchange of C and N between the atmosphere and silicate melts was calculated based on their solubilities, which are determined by vapor pressure. Carbon dissolution as either anhydrous CO_3^{2-} or CO was calculated following H. Keppler & G. Golabek (2019) using Henry's law constants from H. Ni & H. Keppler (2013; $K_{\mathrm{CO}} = 0.016$ ppm MPa^{-1}) and T. Yoshioka et al. (2019; $K_{\mathrm{CO2}} = 0.155$ ppm MPa^{-1}), respectively. The concentration of carbon in the MO (C_C^{MO}) was determined by

$$C_C^{\mathrm{MO}} = K_{\mathrm{CO}}.f\mathrm{CO} + K_{\mathrm{CO_2}}.f\mathrm{CO_2},$$

where fCO and $f\mathrm{CO}_2$ represent the fugacities of CO and CO_2, respectively, in the vapor phase.

The fugacities were calculated based on the equilibrium reaction:

$$\mathrm{CO_{(g)}} + \tfrac{1}{2}\,\mathrm{O_{2(g)}} = \mathrm{CO_{2(g)}}.$$

The equilibrium thermodynamic parameters were calculated from

$$\Delta G^{T,P} = G_f^{T,1\,\mathrm{bar}}(\mathrm{CO_2}) - G_f^{T,1\,\mathrm{bar}}(\mathrm{CO}) + RT\,\ln f\mathrm{CO_2} - \tfrac{1}{2}RT\,\ln f\mathrm{O_2} - RT\,\ln f\mathrm{CO} = 0,$$

where $\Delta G^{T,P}$ is the change in Gibbs free energy at any P and T and is 0 at equilibrium. The standard Gibbs free energy of the formation values for CO_2 and CO ($G_f^{T,1\,\mathrm{bar}}$ (CO_2) and $G_f^{T,1\,\mathrm{bar}}$(CO)) were obtained using NIST-JANAF thermochemical tables.[3]

---

[3] https://janaf.nist.gov/

For N, we used the two-species model from G. Libourel et al. (2003) to determine N solubility in the silicate melts under both oxidized and reduced conditions, based on the partial pressure of N (pN) and fO_2:

$$C_{\mathrm{N}}^{\mathrm{MO}} = 0.06 p_{\mathrm{N}} + 5.97 {p_{\mathrm{N}}}^{1/2} f\mathrm{O}_2{}^{-3/4},$$

where $C_{\mathrm{N}}^{\mathrm{MO}}$ represents the concentration of N in the MO.

For S, we applied a fixed Henrian constant, $S_{\mathrm{S}} = 5000\,\mu\mathrm{g\,g^{-1}\,MPa^{-1}}$, to account for S dissolved as various sulfurous species like S_2 and H_2S (M. M. Hirschmann 2016). Since the solubilities of Se and Te in silicate melts are not well established, we used a Henry's law constant similar to that of S to estimate their solubilities in our models.

ORCID iDs

Damanveer S. Grewal https://orcid.org/0000-0002-5653-1543
Varun Manilal https://orcid.org/0009-0009-2950-0248

References

Abernethy, F. A. J., Verchovsky, A. B., Franchi, I. A., & Grady, M. M. 2018, M&PS, 53, 375
Albarède, F. 2009, Natur, 461, 1227
Alexander, C. M. O. 2022, GeCoA, 318, 428
Alexander, C. M. O., Bowden, R., Fogel, M. L., et al. 2012, Sci, 337, 721
Alexander, C. M. O., Russell, S. S., Arden, J. W., et al. 1998, M&PS, 33, 603
Armstrong, K., Frost, D. J., McCammon, C. A., Rubie, D. C., & Boffa Ballaran, T. 2019, Sci, 365, 903
Benedikt, M. R., Scherf, M., Lammer, H., et al. 2020, Icar, 347, 113772
Bernadou, F., Gaillard, F., Füri, E., Marrocchi, Y., & Slodczyk, A. 2021, ChGeo, 573, 120192
Blanchard, I., Rubie, D. C., Jennings, E. S., et al. 2022, E&PSL, 580, 117374
Bottke, W. F., Walker, R. J., Day, J. M. D., Nesvorny, D., & Elkins-Tanton, L. 2010, Sci, 330, 1527
Boujibar, A., Andrault, D., Bouhifd, M. A., et al. 2014, E&PSL, 391, 42
Brasser, R., Mojzsis, S. J., Werner, S. C., Matsumura, S., & Ida, S. 2016, E&PSL, 455, 85
Braukmüller, N., Wombacher, F., Funk, C., & Münker, C. 2019, NatGe, 12, 564
Budde, G., Burkhardt, C., & Kleine, T. 2019, NatAs, 3, 736
Canup, R. M. 2004, Icar, 168, 433
Canup, R. M., & Asphaug, E. 2001, Natur, 412, 708
Chi, H., Dasgupta, R., Duncan, M. S., & Shimizu, N. 2014, GeCoA, 139, 447
Chou, C.-L. 1978, LPSC, 9, 219
Dalou, C., Hirschmann, M. M., von der Handt, A., Mosenfelder, J., & Armstrong, L. S. 2017, E&PSL, 458, 141
Dasgupta, R., Falksen, E., Pal, A., & Sun, C. 2022, GeCoA, 336, 291
Dasgupta, R., & Grewal, D. S. 2019, in Deep Carbon: Past to Present, ed. B. Orcutt et al. (Cambridge: Cambridge Univ. Press), 4
Dauphas, N. 2017, Natur, 541, 521
Day, J. M. D., Brandon, A. D., & Walker, R. J. 2015, RvMG, 81, 161
Day, J. M. D., Pearson, D. G., & Taylor, L. A. 2007, Sci, 315, 217
Deng, J., Du, Z., Karki, B. B., Ghosh, D. B., & Lee, K. K. M. 2020, NatCo, 11, 2007
Erkaev, N. V., Lammer, H., Elkins-Tanton, L. T., et al. 2014, P&SS, 98, 106
Fischer, R. A., Cottrell, E., Hauri, E., Lee, K. K. M., & Le Voyer, M. 2020, PNAS, 117, 8743
Fischer-Gödde, M., Elfers, B-M., Münker, C., et al. 2020, Natur, 579, 240
Fischer-Gödde, M., & Kleine, T. 2017, Natur, 541, 525
Foustoukos, D. I., Alexander, D., & Cody, G. D. 2021, GeCoA, 300, 44
Fu, R. R., & Elkins-Tanton, L. T. 2014, E&PSL, 390, 128
Fu, R. R., Young, E. D., Greenwood, R. C., & Elkins-Tanton, L. T. 2017, in Planetesimals, ed. L. T. Elkins-Tanton & B. P. Weiss (Cambridge: Cambridge Univ. Press), 115
Genda, H., Brasser, R., & Mojzsis, S. J. 2017, E&PSL, 480, 25
Grady, M. M., & Wright, I. P. 2003, SSRv, 106, 231
Grewal, D. S. 2022, ApJ, 937, 123
Grewal, D. S., & Asimow, P. D. 2023, GeCoA, 344, 146
Grewal, D. S., Bhattacharjee, S., Mardaru, G.-D., & Asimow, P. D. 2025, GeCoA, 388, 34
Grewal, D. S., Dasgupta, R., & Aithala, S. 2021a, E&PSL, 571, 117090
Grewal, D. S., Dasgupta, R., & Farnell, A. 2020, GeCoA, 280, 281
Grewal, D. S., Dasgupta, R., Holmes, A. K., et al. 2019a, GeCoA, 251, 87
Grewal, D. S., Dasgupta, R., Hough, T., & Farnell, A. 2021b, NatGe, 14, 369
Grewal, D. S., Dasgupta, R., & Marty, B. 2021c, NatAs, 5, 356
Grewal, D. S., Dasgupta, R., Sun, C., Tsuno, K., & Costin, G. 2019b, SciA, 5, eaau3669
Grewal, D. S., Miyazaki, Y., & Nie, N. X. 2024a, PSJ, 5, 181
Grewal, D. S., Nie, N. X., Zhang, B., Izidoro, A., & Asimow, P. D. 2024b, NatAs, 8, 290
Grewal, D. S., Seales, J. D., & Dasgupta, R. 2022a, E&PSL, 598, 117847
Grewal, D. S., Sun, T., Aithala, S., et al. 2022b, GeCoA, 338, 347
Le Guillou, C., Bernard, S., Brearley, A. J., & Remusat, L. 2014, GeCoA, 131, 368
Hashizume, K., & Sugiura, N. 1998, M&PS, 33, 1181
Hirschmann, M. M. 2016, AmMin, 101, 540
Hirschmann, M. M. 2018, E&PSL, 502, 262
Hirschmann, M. M. 2022, GeCoA, 328, 221
Hirschmann, M. M., Bergin, E. A., Blake, G. A., Ciesla, F. J., & Li, J. 2021, PNAS, 118, e2026779118
Huang, D., Siebert, J., Sossi, P., et al. 2024, GeCoA, 376, 100
Jackson, C. R. M., Cottrell, E., Du, Z., Bennett, N. R., & Fei, Y. 2021, GChPL, 18, 37
Keppler, H., & Golabek, G. 2019, GChPL, 11, 12
Kimura, K., Lewis, R. S., & Anders, E. 1974, GeCoA, 38, 683
Korenaga, J., & Marchi, S. 2023, PNAS, 120, e2309181120
Kuwahara, H., Nakada, R., Kadoya, S., Yoshino, T., & Irifune, T. 2023, NatGe, 16, 461
Labidi, J., Cartigny, P., & Moreira, M. 2013, Natur, 501, 208
Lammer, H., Scherf, M., Kurokawa, H., et al. 2020, SSRv, 216, 74
Landeau, M., Deguen, R., Phillips, D., et al. 2021, E&PSL, 564, 116888
Laurenz, V., Rubie, D. C., Frost, D. J., & Vogel, A. K. 2016, GeCoA, 194, 123
Li, Y., Dasgupta, R., & Tsuno, K. 2015, E&PSL, 415, 54
Li, Y., Dasgupta, R., Tsuno, K., Monteleone, B., & Shimizu, N. 2016, NatGe, 9, 781
Li, Y., Wiedenbeck, M., Monteleone, B., et al. 2023, E&PSL, 605, 118032
Libourel, G., Marty, B., & Humbert, F. 2003, GeCoA, 67, 4123
Lichtenberg, T., Golabek, G. J., Burn, R., et al. 2019, NatAs, 3, 307
Mann, U., Frost, D. J., Rubie, D. C., Becker, H., & Audétat, A. 2012, GeCoA, 84, 593
Marchi, S., Canup, R. M., & Walker, R. J. 2018, NatGe, 11, 77
Marty, B., Almayrac, M., Barry, P. H., et al. 2020, E&PSL, 551, 116574
Mathias, D. L., Wheeler, L. F., & Dotson, J. L. 2017, Icar, 289, 106
Meisel, T., Walker, R. J., & Morgan, J. W. 1996, Natur, 383, 517
Nakajima, M., Golabek, G. J., Wünnemann, K., et al. 2021, E&PSL, 568, 116983
Newcombe, M. E., Nielsen, S. G., Peterson, L. D., et al. 2023, Natur, 615, 854
Ni, H., & Keppler, H. 2013, RvMG, 75, 251
O'Neill, H. St C. 1991, GeCoA, 55, 1159
Pearson, V. K., Sephton, M. A., Franchi, I. A., Gibson, J. M., & Gilmour, I. 2006, M&PS, 41, 1899
Peterson, L. D., Newcombe, M. E., Alexander, C. M. O., et al. 2023a, GeCoA, 340, 141
Peterson, L. D., Newcombe, M. E., Alexander, C. M. O., et al. 2023b, E&PSL, 620, 118341
Peterson, L. D., Newcombe, M. E., Alexander, D., Wang, J., & Nielsen, S. G. 2024, GeCoA, 370, 1
Rai, N., & Van Westrenen, W. 2014, E&PSL, 388, 343
Rose-Weston, L., Brenan, J. M., Fei, Y., Secco, R. A., & Frost, D. J. 2009, GeCoA, 73, 4598
Rubie, D. C., Frost, D. J., Mann, U., et al. 2011, E&PSL, 301, 31
Rubie, D. C., Jacobson, S. A., Morbidelli, A., et al. 2015, Icar, 248, 89
Rubie, D. C., Laurenz, V., Jacobson, S. A., et al. 2016, Sci, 353, 1141
Sarafian, A. R., John, T., Roszjar, J., & Whitehouse, M. J. 2017, E&PSL, 459, 311
Schlichting, H. E., Sari, R., & Yalinewich, A. 2015, Icar, 247, 81
Sephton, M. A., Verchovsky, A. B., Bland, P. A., et al. 2003, GeCoA, 67, 2093
Shi, L., Lu, W., Kagoshima, T., et al. 2022, NatCo, 13, 4769
Speelmanns, I. M., Schmidt, M. W., & Liebske, C. 2019, E&PSL, 510, 186
Suer, T.-A., Jackson, C., Grewal, D. S., Dalou, C., & Lichtenberg, T. 2023, FrEaS, 11, 1159412
Suer, T. A., Siebert, J., Remusat, L., Menguy, N., & Fiquet, G. 2017, E&PSL, 469, 84
Sugiura, N., Arkani-Hamed, J., & Strangway, D. W. 1986, E&PSL, 78, 148
Tagawa, S., Sakamoto, N., Hirose, K., et al. 2021, NatCo, 12, 2588
Tsuno, K., Grewal, D. S., & Dasgupta, R. 2018, GeCoA, 238, 477
Tsuno, K., Grewal, D. S., Xu, V., et al. 2024, GeoRL, 51, e2024GL109584

Varas-Reus, M. I., König, S., Yierpan, A., Lorand, J-P., & Schoenberg, R. 2019, NatGe, 12, 779
Walker, R. J. 2009, Geoch, 69, 101
Wang, Z., & Becker, H. 2013, Natur, 499, 328
Weidenschilling, S. J. 2011, Icar, 214, 671
Weidenschilling, S. J. 2019, M&PS, 54, 1115
Woo, J. M. Y., Genda, H., Brasser, R., & Mojzsis, S. J. 2019, Icar, 333, 87
Yoshioka, T., Nakashima, D., Nakamura, T., Shcheka, S., & Keppler, H. 2019, GeCoA, 259, 129
Young, E. D., Shahar, A., & Schlichting, H. E. 2023, Natur, 616, 306